

Landing Site Searching and Selection Algorithm Development Using Vision System and Its Application to Quadrotor

Jongho Park, Youdan Kim, *Member, IEEE*, and Sungwan Kim, *Senior Member, IEEE*

Abstract—An enhanced search algorithm of a landing site on unknown terrain using stereo vision information for a quadrotor unmanned aerial vehicle is developed. For the development, a quadrotor dynamic model, including nonlinear actuator dynamics, is constructed and guidance and control system is designed based on feedback linearization and linear quadratic tracker. Stereo vision sensor is used to acquire depth map information of the terrain and flatness information of the topography is obtained by extracting the edge of the depth map and performing Euclidean distance transform. Energy consumption of the quadrotor is also considered. The three measures of: 1) the depth; 2) the flatness; and 3) the energy consumption are combined to propose a performance index to determine the safe landing spot of the quadrotor. Numerical simulation is performed to verify the performance of the proposed algorithm and hardware system applicable to practical implementation is also included.

Index Terms—Autonomous landing, depth map, quadrotor system, stereo vision, unmanned aerial vehicle (UAV).

I. INTRODUCTION

RESEARCH on the development of unmanned aerial vehicle (UAV) has been getting great attention due to the market growth based on various advantages. As an example, the U.S. military UAV market is expected to grow at a 12% compound annual growth rate reaching \$18.7 billion in 2018 [1]. Over the forecast period of 2013–2018, the cumulative U.S. military UAV market is projected to generate the total of \$86.5 billion revenues. To build a high-fidelity UAV, broad researches have been actively performed to develop a fully autonomous function of UAV in recent decades [2]. A high-fidelity UAV will enable advanced missions, including surveillance, reconnaissance, exploration, delivery, disaster assistance, and so on.

To accomplish the UAV mission successfully, it is extremely important to find a suitable, flat landing site while considering

Manuscript received January 5, 2014; accepted June 14, 2014. Date of publication August 27, 2014; date of current version February 11, 2015. Manuscript received in final form June 29, 2014. This work was supported by the Unmanned Technology Research Center, Korea Advanced Institute of Science and Technology, Daejeon, Korea, through the DAPA and the Agency for Defense Development. Recommended by Associate Editor M. Mattei.

J. Park and Y. Kim are with the Department of Mechanical and Aerospace Engineering, Institute of Advanced Aerospace Technology, Seoul National University, Seoul 151-742, Korea (e-mail: parkjo05@snu.ac.kr; ydkim@snu.ac.kr).

S. Kim is with the College of Medicine, Seoul National University, Seoul 110-799, Korea (e-mail: sungwan@snu.ac.kr).

Color versions of one or more of the figures in this paper are available online at <http://ieeexplore.ieee.org>.

Digital Object Identifier 10.1109/TCST.2014.2341214

energy consumption and safety. However, during the mission, the UAV could be ended-up with landing on undesignated or unspecified area in case of mechanical failure or subsystem failure, including fuel shortage. Further, it may have to land on the populated area or even on foe's territory in case of emergency situations. While the easily detected flat regions may be promising candidates for a landing [3], appropriate landing site should be carefully searched before landing in case of unknown territory where the special patterns or features do not exist in general. Therefore, an adequate landing site searching algorithm without using the patterns and/or features should be developed.

In this context, various researches on the landing site searching and selection have been conducted especially for a robotic spacecraft landing on the Mars or Moon [4]–[8]. Some works using vision sensors are [9]–[11]. Strandmoe *et al.* [9] suggested the autonomous landing system based on vision for a planetary lander. Matthies *et al.* [10] developed a landing hazard detection algorithm using stereo vision and performed shadow analysis for landing site selection in the Mars. Parreira *et al.* [11] gathered visibility constraints, fuel consumption, trajectory constraints, and thruster constraints to select a candidate site for vision based landing. Collision avoidance techniques during the landing have been also examined [12]–[14].

On the other hand, there have been various recent research efforts for a successful landing of UAVs and most of them have used vision sensors [15]–[23] in estimating runway position and distance from the UAV, detecting edges of runway. Further, other approach involves multistage neural network classification technique to classify candidate landing sites for UAV [24]. A special maneuver, such as aggressive landing of three degrees of freedom helicopter, was examined in [25].

In this research, a suitable, flat landing site is searched with vision sensor information. Active sensor, such as light detection and ranging was used by Johnson and SanMartin to propose terrain relative navigation algorithm for autonomous comet landing [26], [27]. While the active sensor provides accurate information, they are expensive and heavy. This is why passive vision sensor, such as camera, is gaining popularity in the field of UAVs due to its low cost and light weight [28]. A camera system has been widely applied for the estimation of attitude and position of UAV, reconstruction of 3-D map, obstacle detection problem, path planning, and

navigation [29]–[37]. In this paper, stereo camera system is used to obtain 3-D image.

Quadrotor UAV is considered in this research among various UAVs because of its considerable advantages over fixed-wing UAVs and conventional rotary-wing UAVs for many applications. For instance, the capability of vertical takeoff and landing (VTOL) enables launch and recovery system with minimum space. In addition, it is capable of hovering over a specified place as well as performing longitudinal and lateral flight. These properties of the quadrotor are advantageous in the congested areas, such as indoor places and urban environments. This vehicle has a special structure of the cross configuration of two rods with four rotors. Unlike a helicopter, since the quadrotor balances itself using the counter rotating rotors, a tail rotor is not required that eventually leads to the reduction of the contact hazard. Even though the structure of the quadrotor is not quite complicated, it is indeed a highly nonlinear underactuated system [38], [39]. Therefore, designing a guidance and control system is quite a challenge.

In this paper, a stereo vision-based landing site searching and selection algorithm is proposed; which includes modeling of the quadrotor, controller design, and maneuvers, from the hovering in midair to touchdown on a suitable, flat landing site. The quadrotor is modeled through Newton–Euler equations considering the nonlinearities of the actuator [38], [40]–[43]. The feedback linearization is adopted to design nonlinear controller [44]. The overall control system is separated into attitude and position subsystems, and linear quadratic tracker is applied to design control system [45]. To deal with the underactuated problem of the quadrotor, the outputs of the attitude control subsystem are considered as virtual inputs of the position control subsystem [42], [46], [47]. For the search of landing site, it is assumed that the quadrotor is equipped with two cameras pointing downward to acquire the stereo vision images. The decision making map being consisted of the evaluated depth map, flatness map, and energy consumption map is considered to find the most appropriate landing spot for the quadrotor. The depth map can be obtained by the stereo vision image [48], and the flatness map is constructed by extracting the edge of the depth map using Canny method [49], [50] and performing the distance transform method [51]. In this research, it is shown that the energy consumption map [52] could be replaced by the distance map to resolve the problem of the computational load. Extensive numerical simulation is performed to verify the performance of the proposed stereo vision-based landing site searching algorithm. The result shows that the performance is quite improved with respect to both in computation time and energy consumption, compared with the previous result [53]. Experimental systems, which include vision system, flight control system, and quadrotor system, are also introduced for practical implementation.

The contributions of this paper can be summarized as follows. First, a searching algorithm to find a proper landing site for a quadrotor system has been developed and this method could be used to find a landing site on complete unknown terrain in real-time. Second, a depth map obtained by the image from stereo cameras on the quadrotor could be utilized to obtain distance information from a quadrotor to the ground

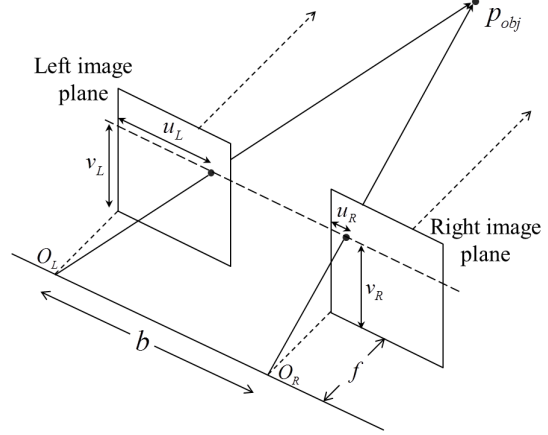


Fig. 1. Structure of stereo vision system.

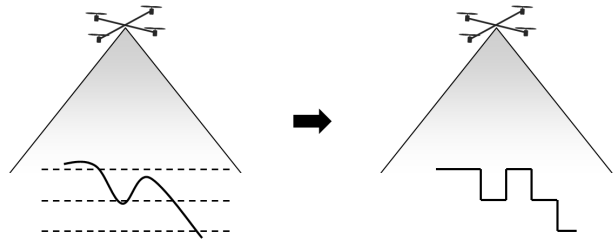


Fig. 2. Left: true topography. Right: corresponding depth map.

and the depth map information could be also used in determining the appropriateness of the landing. Third, a decision making map is proposed by considering the following three constraints: 1) the depth; 2) the flatness of the candidate landing site; and 3) the energy consumption required to land on the candidate landing site from the current position. Using the proposed decision making map, the performance of the landing site search can be significantly improved with respect to both in computation time and energy consumption.

This paper is organized as follows. The concept of depth map is explained in Section II. In Section III, landing site searching algorithm is presented and simulation results are given in Section IV followed by conclusion in Section V. Quadrotor system modeling and hardware system are addressed in Appendixes A and B, respectively.

II. DEPTH MAP OF STEREO VISION

A. Depth Map Modeling

In a monocular camera system, a real object in 3-D space is projected onto an image plane which is a 2-D space. As a result, the information of distance in the direction of projection is lost when only one camera is used. On the other hand, the information of distance can be obtained by computing a depth map if a stereo vision is used. Depth map is an image whose pixels have the information of the distance of the object from a viewpoint.

Fig. 1 shows the structure of the stereo vision system. In Fig. 1, b is a baseline, f is a focal length, P_{obj} is the location of object, and (u_L, v_L) and (u_R, v_R) are points on the

TABLE I
RELATIONSHIP BETWEEN DISPARITY AND DEPTH

Disparity	1	2	3	4	5	6	7	8	9
Depth (m)	71.87	35.94	23.96	17.97	14.37	11.98	10.27	8.98	7.99

10	11	12	13	14	15	16	17	18	19	20
7.19	6.53	5.99	5.53	5.13	4.79	4.49	4.23	3.99	3.78	3.59
21	22	23	24	25	26	27	28	29	30	31
3.42	3.27	3.12	3.00	2.87	2.76	2.66	2.57	2.48	2.40	2.32

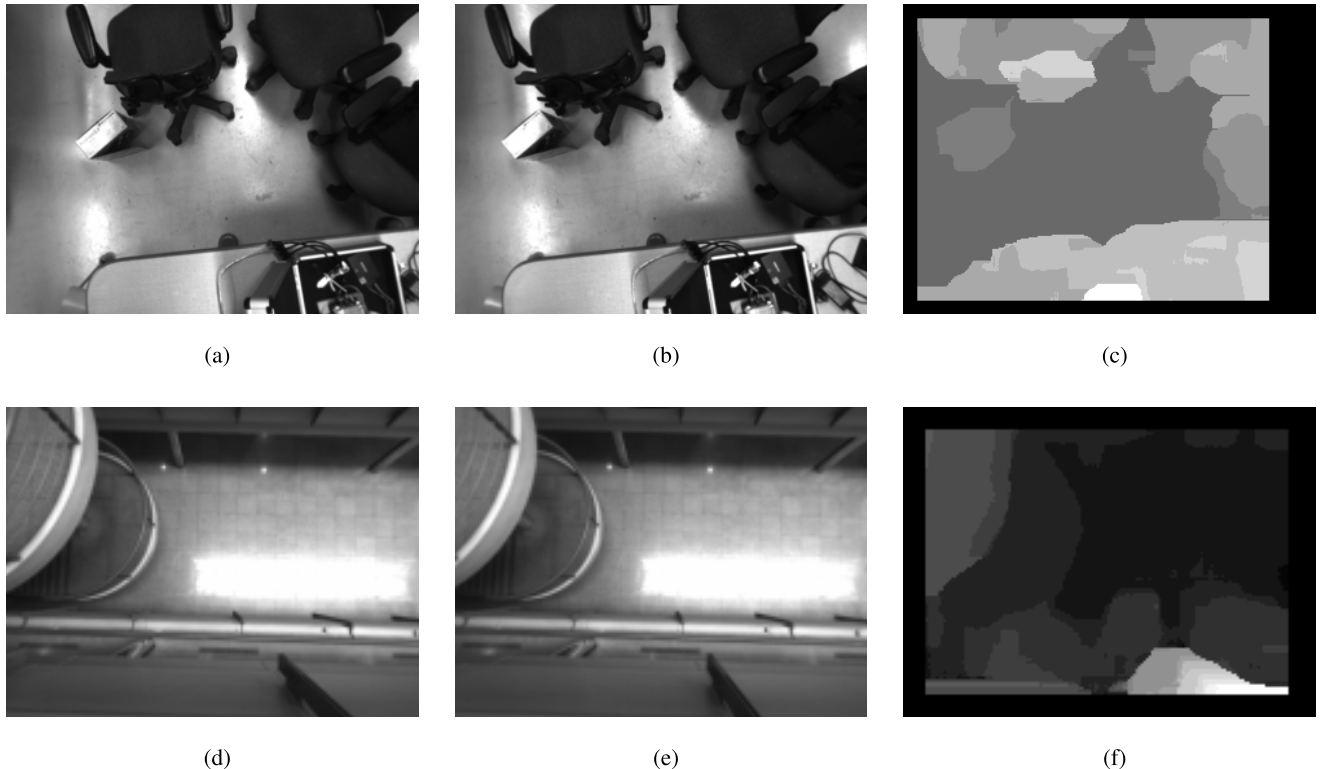


Fig. 3. Depth map obtained by Bumblebee2. (a) Left image (Example 1). (b) Right image (Example 1). (c) Depth map (Example 1). (d) Left image (Example 2). (e) Right image (Example 2). (f) Depth map (Example 2).

left and right image planes, respectively, which are obtained as follows:

$$\begin{bmatrix} u_L \\ v_L \end{bmatrix} = \frac{f}{z} \begin{bmatrix} x - (-b/2) \\ y \end{bmatrix} = \frac{f}{z} \begin{bmatrix} x + b/2 \\ y \end{bmatrix} \quad (1)$$

$$\begin{bmatrix} u_R \\ v_R \end{bmatrix} = \frac{f}{z} \begin{bmatrix} x - b/2 \\ y \end{bmatrix}. \quad (2)$$

Using (1) and (2), we have

$$u_L - u_R = \frac{f}{z}b \quad (3)$$

$$z = \frac{fb}{u_L - u_R} \quad (4)$$

where $u_L - u_R$ and z are disparity and depth, respectively. Note from (4) that the depth can be obtained by using the focal length of the camera, the baseline of the camera, and the disparity of the object.

Disparity refers to the difference in image plane location of the object captured by the left and right cameras of the stereo vision, resulting from the cameras' horizontal separation. It is composed of multiplication of the actual size of the pixel and the pixel difference between the left image and the right image of the object. The latter is a positive integer that means that the depth map does not give the entire information of true topography, as shown in Fig. 2. Dotted lines in Fig. 2 indicates certain depths, and real values merge into these lines.

Table I shows the depths according to the disparities in a certain example case where focal length is 0.01 m, baseline 0.2 m, horizontal field of view 48°, vertical field of view 36.9°, and pixel size 2.75×10^{-5} m. The computed depth map from the images of the stereo vision camera is shown in Fig. 3. For a stereo vision camera, Bumblebee2 is used. Fig. 3(a) and (b) shows the left and right images of the office

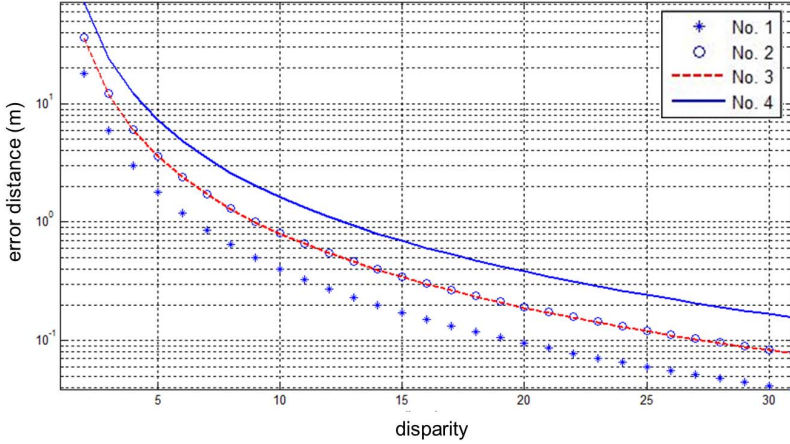


Fig. 4. Error distance for various baselines and focal lengths.

from the ceiling, respectively, and Fig. 3(c) shows the depth map computed from the images. Fig. 3(d)–(f) shows the results using the images inside the building floor from the higher place. The accuracy of the pixel correspondence in the depth map is degraded in the real environment. To cope with this problem, pixels with no correspondence due to the imperfect matching are filled with the depth values of the pixels adjacent to them. The darker the image is, the closer the terrain is to the quadrotor, which means that the depth is smaller.

B. Performance Analysis of Depth Map

Error performance must be analyzed since the depth does not give the true value. Let us define D_k and DP_k as k th disparity and depth value with $k \in \{1, 2, \dots, n\}$, respectively. The k th disparity D_k consists of the depth from the average value between DP_{k-1} and DP_k to the average value between DP_k and DP_{k+1} . If the actual distance of p_{obj} from the stereo vision is d_p , then its disparity in the depth map can be obtained as follows:

$$D_k = \arg \min_m \{ \| d_p - DP_m \| \mid m \in \{1, 2, \dots, n\} \}. \quad (5)$$

For example, in Table I, depths from 5.76 to 6.26 m correspond to D_{12} . In other words, D_{12} has the error distance of $-0.23 < e_z < 0.27$ m. Error distance varies considerably through the whole disparity. Note that the gap between the depths is wide when the disparity is small. In addition, the gap becomes narrower as the disparity gets bigger, as shown in Fig. 3. In the lighter parts of the image, the gap between boundaries is relatively wide. On the other hand, as it becomes darker, the gap gets narrower.

The parameters of the stereo vision can influence the error distance of the depth map. Table II shows four different cases depending on the focal length and the baseline of the stereo vision camera, and Fig. 4 shows the error distances of these cases with respect to disparities. As shown in Fig. 4, the error distance reduces as the disparity gets bigger. In addition, if the baseline or the focal length increases, the error distance increases.

Let us define H_{fov} and V_{fov} as the horizontal and vertical field of view of the camera, respectively. In addition, ℓ_h and ℓ_v

TABLE II
FOUR CASES OF CAMERA PARAMETERS

No.	b	f	H_{fov}	V_{fov}	resolution
1	0.1m	0.01m	48°	36.93°	360 × 240
2	0.1m	0.02m	24.81°	18.74°	360 × 240
3	0.2m	0.01m	48°	36.93°	360 × 240
4	0.2m	0.02m	24.81°	18.74°	360 × 240

are defined as the horizontal and vertical width of the sensor, respectively. Because H_{fov} and V_{fov} , in Table II, are changed due to the relationships between the field of view and the focal length, they can be represented as follows:

$$H_{\text{fov}} = 2 \arctan \left(\frac{\ell_h}{2f} \right) \quad (6)$$

$$V_{\text{fov}} = 2 \arctan \left(\frac{\ell_v}{2f} \right). \quad (7)$$

If the error distance is increased, the maximum distance covered by the stereo vision increases. This means that objects of further distance can be estimated. However, if the error distance is increased by extending the focal length, the field of view of the camera reduces, as shown in Table II and (6) and (7). If the error distance is increased by extending the baseline, the scene overlapped by two cameras reduces. Both cases indicate the reduction of a given scene that is imaged by the stereo vision.

III. LANDING SITE SEARCHING ALGORITHM UTILIZING STEREO VISION DEPTH MAP

A. Depth Information

Depth information can be utilized in searching the landing site for the quadrotor. When the altitude of the quadrotor is high, insufficient and inaccurate information may be obtained from the depth map. As the quadrotor lowers its altitude, the error distance of the depth map reduces that leads to the

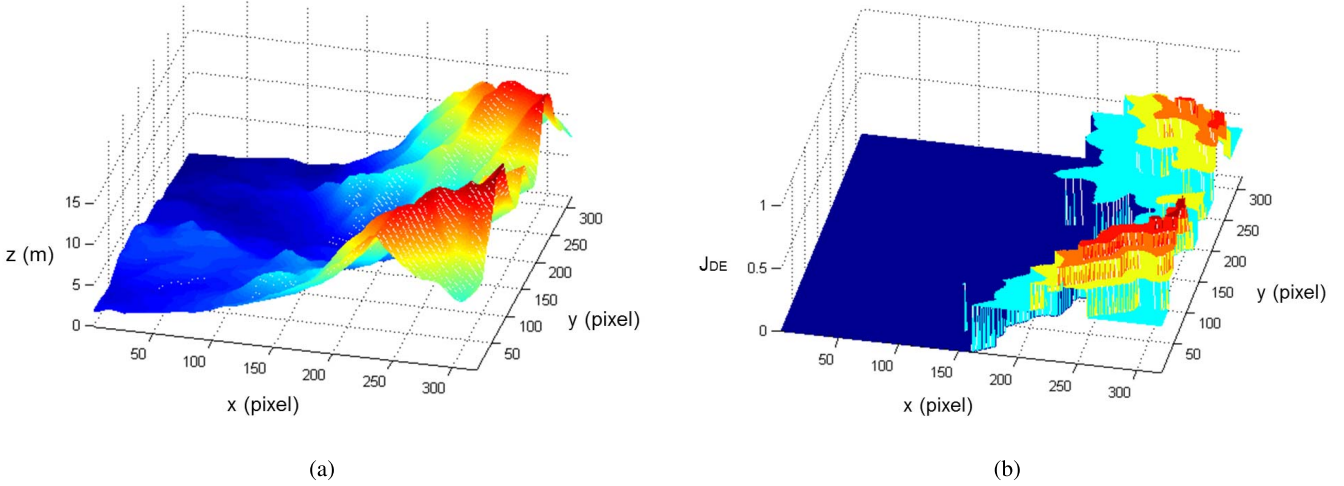


Fig. 5. Terrain and depth information. (a) True terrain. (b) Evaluated depth map.

increase of the depth map accuracy. Therefore, the quadrotor should descend until enough information can be obtained to determine whether or not the spot satisfies a landing condition.

As the height (z -direction) of the quadrotor above the terrain decreases, the error distance of the depth map decreases and its accuracy increases. Therefore, a pixel with larger disparity includes more accurate information for landing, and therefore, it must be evaluated by assigning higher score than a pixel with smaller disparity. If all the other conditions are equal, the quadrotor prefers higher region.

The score of the depth map $J_{DE} \in [0, 1]$ is represented by the map whose x - and y -components refer to the resolution of the image plane and z -component refers to the score of each pixel. The map shows how appropriate the region is for the quadrotor to land with scores $J_{DE} = 1$ most appropriate area, $J_{DE} = 0$ inappropriate area.

Fig. 5(a) shows the true terrain captured by the stereo vision sensor of the quadrotor in midair and Fig. 5(b) shows the corresponding depth evaluation map. Note that the higher region in Fig. 5(a) has a higher score, as shown in Fig. 5(b).

B. Flatness Information

Flatness is the most important element of landing for a VTOL UAV. The area must be flat enough for the quadrotor not to slip, and it must be large enough for landing. Using the obtained depth map, the quadrotor has to select the best spot considering the flatness and largeness.

When the depth map of a topography, including ground obstacles is obtained, the flatness of the area can be represented by the portion having same depth. In fact, having a same level of the depth in the depth map does not guarantee exact same altitude in an actual topography. However, it is the most probable method to judge the flatness with limited information. The largeness of the area can be determined by drawing an inscribed circle in every portion of the image with same depth level, and selecting one that has the largest diameter.

There are many edge detectors of the image, which include methods proposed in [48] and [49]. In this paper,

Canny edge detection algorithm is adopted to extract the edge from the depth map because it performs better than all other detectors for almost all the scenarios [50]. It is a Gaussian based detector that has good performance especially in noise conditions, whereas Prewitt and Sobel detectors are sensitive to noise and provide less accurate results than Canny detector. Canny detector uses a derivative estimation filter based on a linear continuous model, which optimizes the combination of three criteria: 1) signal-to-noise ratio; 2) localization; and 3) low-false positives. Since the Canny edge detector is susceptible to noise in image data, a Gaussian filter is applied to the depth map as follows:

$$G(x, y) = \frac{1}{2\pi\sigma^2} e^{-\frac{x^2+y^2}{2\sigma^2}} \quad (8)$$

where x and y are pixel elements in the depth map, and σ is the standard deviation of the Gaussian filter, which is set to $\sqrt{2}$ in this paper. Since the depth map image has two dimensions, an edge has an orientation. The edge orientation and its magnitude can be obtained as follows:

$$\angle G = \arctan(G(y)/G(x)) \quad (9)$$

$$|G| = \sqrt{G(x)^2 + G(y)^2}. \quad (10)$$

Then, the stage referred to as nonmaximum suppression is carried out to determine a set of edge points. Finally, these edges are traced through the image using thresholding with hysteresis. By applying the Canny edge detector, the depth map becomes binary image where nonzero elements represent the edge.

To find the inscribed circle, a distance transform method is adopted. The distance transform assigns a number to each pixel that refers to the distance between the corresponding pixel and the nearest nonzero pixel of the binary image. Euclidean distance, $((x_1 - x_2)^2 + (y_1 - y_2)^2)^{1/2}$, is used between the pixel (x_1, y_1) and (x_2, y_2) . For each pixel p in the image plane, the Euclidean distance transform performs as



Fig. 6. Extracting flatness information. (a) Actual terrain. (b) Depth map. (c) Edge extraction. (d) Distance transform.

follows:

$$di(p) = \min_k \left\{ \sqrt{(p - q_k)^T (p - q_k)} \mid B(q_k) = 1 \forall 1 \leq k \leq S \right\} \quad (11)$$

where $B()$ denotes the value of a pixel in the binary image, and k lists all S pixels in the binary image. For example, let us consider the following binary image:

$$bi = \begin{bmatrix} 0 & 0 & 0 & 0 & 0 \\ 0 & 0 & 0 & 1 & 1 \\ 0 & 0 & 0 & 0 & 0 \\ 0 & 1 & 0 & 0 & 0 \\ 0 & 0 & 0 & 0 & 0 \end{bmatrix}. \quad (12)$$

Computing the Euclidean distance transform gives the following matrix:

$$di(bi) = \begin{bmatrix} \sqrt{10} & \sqrt{5} & \sqrt{2} & 1 & 1 \\ \sqrt{5} & 2 & 1 & 0 & 0 \\ \sqrt{2} & 1 & \sqrt{2} & 1 & 1 \\ 1 & 0 & 1 & 2 & 2 \\ \sqrt{2} & 1 & \sqrt{2} & \sqrt{5} & 3 \end{bmatrix}. \quad (13)$$

The above processes are shown in Fig. 6, and flatness map J_{FL} can be computed as follows:

$$J_{FL} = di(\text{Canny}(J_{DE})). \quad (14)$$

Using Fig. 6(d) and (14), the radius of the inscribed circle for each pixel can be obtained. Flatter area in the depth map achieves higher score in the evaluated flatness map. If all the other conditions are equal, the quadrotor prefers flatter area regardless of the distance from its current position. Fig. 6 shows the process of the extracting flatness from the obtained images. As shown in Fig. 6(d), the distance information can be obtained from the depth map [Fig. 6(b)]. And Fig. 7 shows the flatness evaluation map for the considered terrain.

C. Energy Consumption Information

If there exist several flat areas, it may be desirable to land on the closer spot, which consumes less energy of the quadrotor. To reflect this condition, energy consumption is considered. To compute the energy consumption J_{EC} [52], the following equation is used and the computed energy consumption is assigned to each pixel of the landing spot:

$$J_{EC} = \int_{t_0}^{t_f} P dt \quad (15)$$

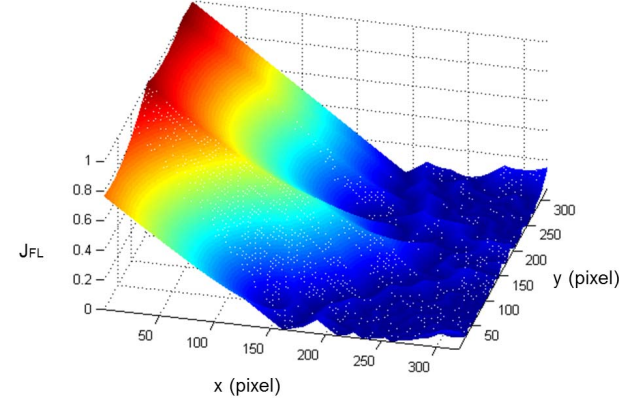


Fig. 7. Evaluated flatness map.

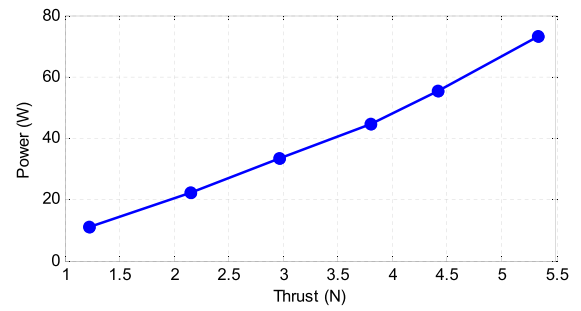


Fig. 8. Relationship between the battery power and the thrust.

where t_0 and t_f correspond to the initial and final time, respectively, and P is a battery power consumption by the thrust force of the quadrotor. The battery power consumed by the quadrotor directly relates to the amount of energy needed to reach the pixel's location. An experiment to identify the relationship between the battery power consumption and the thrust produced by the motor is performed. For the experiment, GAUI 1050KV GUEC GM-410 brushless motor with 10×4.5 in propeller is used, four of which are implemented in our quadrotor system. The result shows that the relationship is almost linear, as shown in Fig. 8. Using this result, the amount of battery power P consumed by the four rotors of the quadrotor can be calculated, and J_{EC} can be obtained using (15).

Fig. 9(a) shows the energy consumption evaluation map for the considered terrain. Higher score refers to less energy consumption.

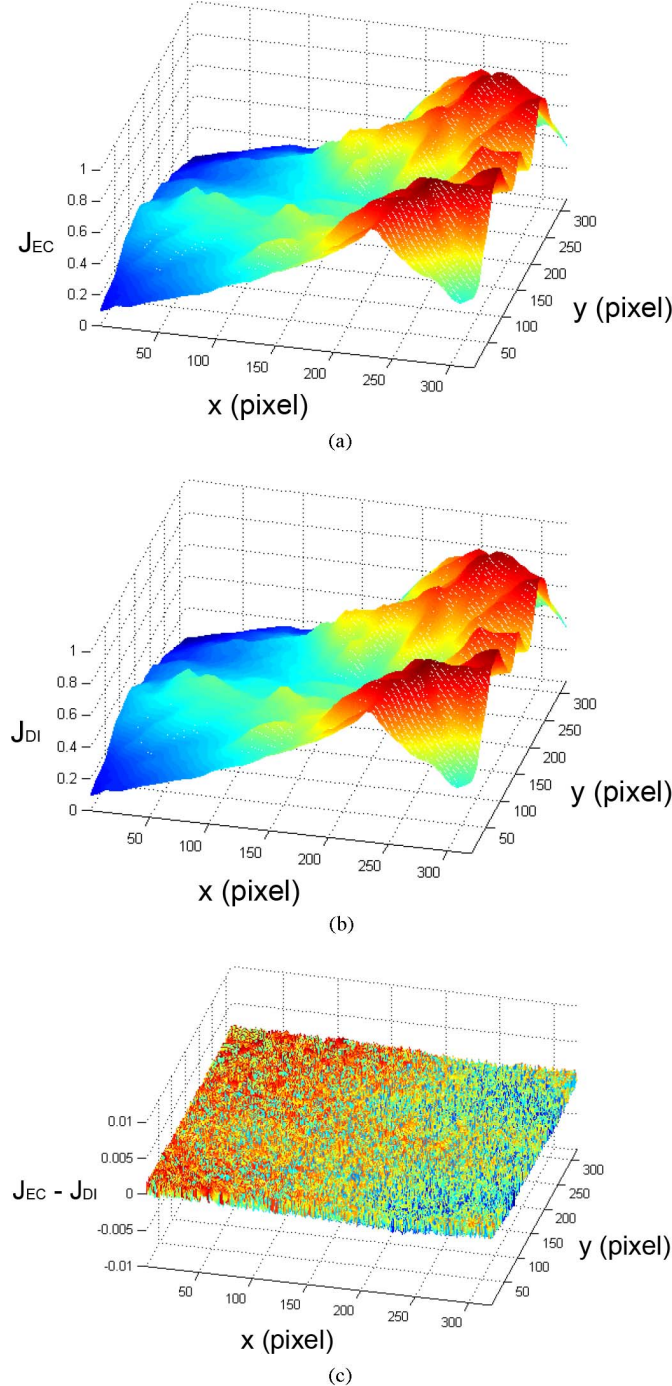


Fig. 9. Energy consumption information. (a) Evaluated energy consumption map. (b) Evaluated distance map. (c) Difference between energy consumption map and distance map.

However, computation load using (15) is huge because the trajectory of the quadrotor must be computed for each pixel. To deal with this problem, an alternative map is introduced. The amount of distance that the quadrotor travels is highly related to the energy consumption of the quadrotor. The distance between the quadrotor and the terrain is computed, and the computed number is assigned to each pixel. Fig. 9(b) shows the distance map J_{DI} . The difference between the energy consumption map of Fig. 9(a) and the distance map

of Fig. 9(b) is shown in Fig. 9(c). The maximum value of the error between two maps is 0.002, which is small compared with the scale of the map. Therefore, distance map J_{DI} can be used instead of energy consumption map J_{EC} that gives significant reduction in computation time.

D. Decision Making Map

The depth map is obtained at each time instant. To determine the landing spot, the evaluated depth map (J_{DE}), the flatness

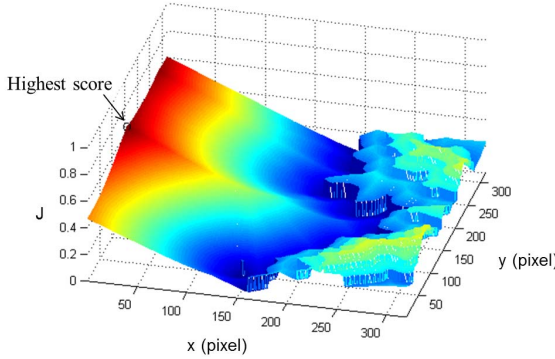


Fig. 10. Combination of evaluated maps.

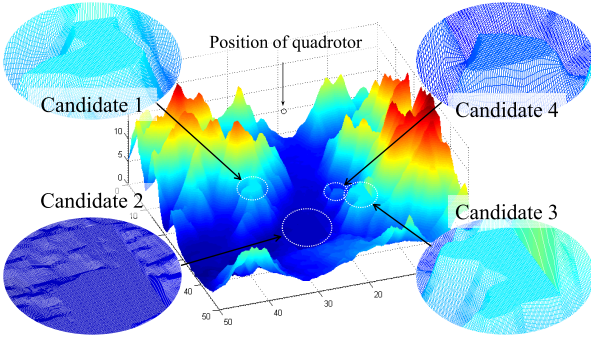


Fig. 11. Four candidate landing sites.

map (J_{FL}), and the distance map (J_{DI}) are combined into one map (J)

$$J = c_1 J_{DE} + c_2 J_{FL} + c_3 J_{DI}, \quad c_1 + c_2 + c_3 = 1 \quad (16)$$

where c_1 , c_2 , and c_3 are weighting parameters for each map. In this paper, c_2 has larger value than c_1 or c_3 because of the importance of the flatness in landing. In general, the following relationship is reasonable among the weighted parameters:

$$c_2 > c_1, \quad c_2 > c_3. \quad (17)$$

However, for a situation that the error distance of the depth map is too large to handle, c_1 should be weighted more. In addition, c_3 can be weighted more in a situation that urgent landing is required due to the lack of energy. Fig. 10 shows the combined map where c_1 , c_2 , and c_3 are set as 0.3, 0.6, and 0.1, respectively. The spot having the highest score in Fig. 10 is the most appropriate area for landing.

Now, let us consider an example to analyze the effectiveness of the weighting parameters. For the purpose of analysis, only four discrete regions are considered as the candidate for landing sites in this particular example, which is shown in Fig. 11. Note that all the pixels inside the image plane should be considered to build the decision making map in the real problem. The quadrotor is in the location of $[28 \ 25 \ 25]^T$. The center locations of candidate 1, 2, 3, and 4 area are $[34 \ 23.5 \ 9]^T$, $[26.5 \ 31 \ 1]^T$, $[15 \ 33 \ 9]^T$, and $[17.5 \ 24.5 \ 5.5]^T$, respectively. The size of flat area of each candidate landing site is ranked in descending order as follows: 2, 3, 4,

TABLE III
SCORE OF FOUR CANDIDATE LANDING SITES

Evaluation type	Candidate 1	Candidate 2	Candidate 3	Candidate 4
Depth map J_{DE}	0.4429	0	0.4429	0.2768
Flatness map J_{FL}	0.1101	0.8018	0.1460	0.1271
Distance map J_{DI}	0.7337	0.4868	0.6480	0.6247

and 1. As shown in Fig. 11, candidate 2 area is slightly coarse.

Each candidate landing site is evaluated through three maps, which are summarized in Table III. In the depth information J_{DE} , the scores of candidates 1 and 3 are equal because of their same height. Candidate 2 is scored zero because the location is the lowest throughout the entire map. In the flatness information J_{FL} , the score reflects the size of flat area. In the distance information J_{DI} , candidates 1 and 2 have the highest score and the lowest score, respectively, because of their distance from the quadrotor.

Table IV summarizes the scores of decision making map based on Table III. The first case is a general case in which the flatness map gets the largest portion. Even though candidate 2 is located in the lowest region, its flat area is significantly larger than any other candidates, and therefore, it is chosen to be the primary landing spot. Case 2 is the case that the emphasis is on energy consumption. In this case, the quadrotor tries to land on the nearest region, and therefore, the quadrotor prefers candidates 1 to 2. In Case 1, candidate 2 is chosen for landing spot. However, as shown in Fig. 11, nearly half of this area is coarse that is not suitable for landing. This coarseness cannot be found from the high location of the quadrotor due to the error distance of the stereo vision. Case 3 points out this phenomenon. By assigning more weight on c_1 , the inherent weakness of the stereo vision can be emphasized. As a result, candidate 2 is considered as the worst landing zone.

If the spot with the highest score in the decision making map is found, the position vector of the spot with respect to the inertial frame is computed so that it can be used as a desired position vector in the position control subsystem. Let us define x_{im} and y_{im} as the x - and y -coordinates of the desired position in the image plane, respectively, and r_x and r_y as the resolution of the camera along the x - and y -axis, respectively. Then, the x - and y -coordinates of the desired position in the inertial frame can be represented as follows:

$$x_h = \frac{(x + z \tan(H_{fov}/2)) \times x_{im}}{r_x} \quad (18)$$

$$y_h = \frac{(y + z \tan(V_{fov}/2)) \times y_{im}}{r_y} \quad (19)$$

where x and y are position coordinates of the quadrotor. In addition, if DP_h is the depth value of the spot with the highest score, z -coordinate of the desired position in the inertial frame can be computed as

$$z_h = z - DP_h \quad (20)$$

where z is position coordinate of the quadrotor.

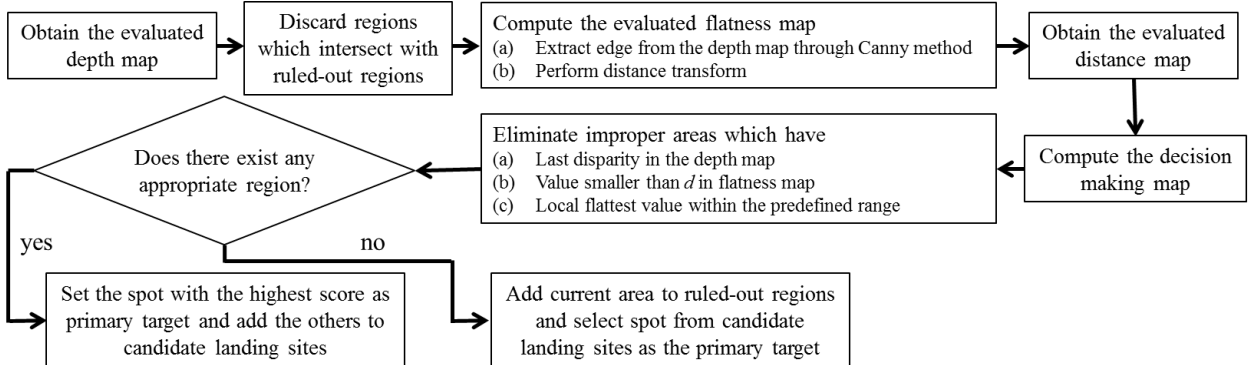


Fig. 12. Flowchart of landing site search algorithm.

TABLE IV
FINAL SCORE OF DECISION MAKING FOR LANDING

	$(c_1 \ c_2 \ c_3)$	Candidate 1	Candidate 2	Candidate 3	Candidate 4
Case 1 : (0.2 0.6 0.2)		0.3014	0.5784	0.3058	0.2566
Case 2 : (0.2 0.2 0.6)		0.5508	0.4524	0.5066	0.4556
Case 3 : (0.6 0.2 0.2)		0.4345	0.2577	0.4245	0.3164

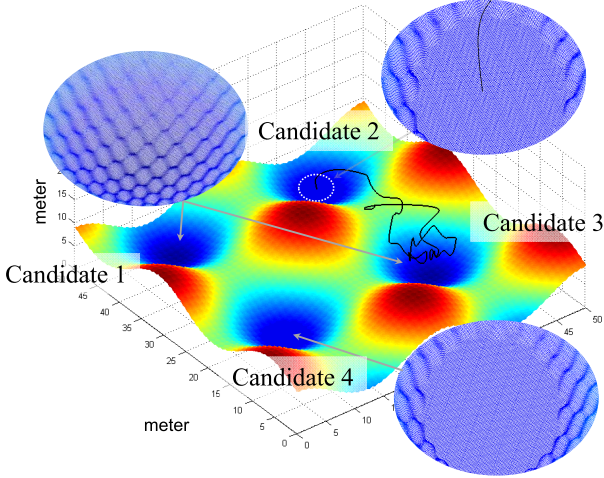


Fig. 13. Terrain and trajectory of the quadrotor (Case 1).

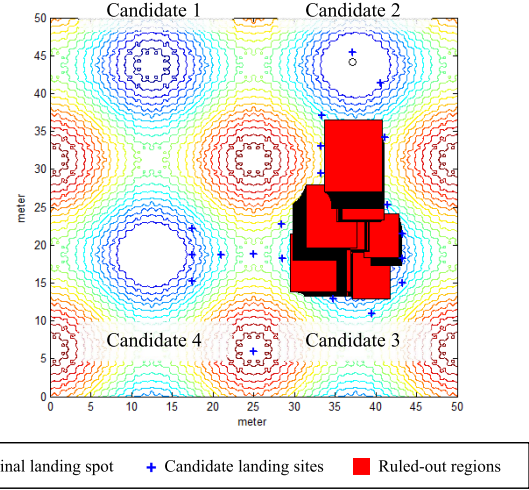


Fig. 14. Contour map (Case 1).

The spot with the highest score should be chosen for the primary candidate landing site. However, the positions of the other possible candidate landing sites have to be also stored for the case that the spot with the highest score is not the appropriate landing site in the end. There may exist many candidate landing sites, which have high score in the decision making map. Storing all these information is not efficient, and therefore, the following procedure is considered in this paper.

First, spots having the last disparity D_n in the depth map should be eliminated, because D_n contains inaccurate information of the heights. For instance, the last disparity D_{31} in Table I includes all the distances that are less than 2.32 m. Second, in the flatness map, the circles whose radii are not large enough to land must be excluded. This can be

determined by comparing the distance from the center of mass of the quadrotor to the rotor axis, d , and the value of a pixel in the evaluated flatness map. Finally, if there is a local flattest spot in the flatness map, other spots within the range of this area need to be eliminated so that no overlapped information is stored. The position vectors of the spots that survive the above procedure are stored.

Now, let us consider the situation that no proper area is found in the current image plane. Then, the current image is regarded as inappropriate area, and the corresponding location is discarded. Since the quadrotor does not find proper landing site in this situation, another spot previously stored in the candidate landing sites is selected as the next primary target. There may be various ways to store the location information.

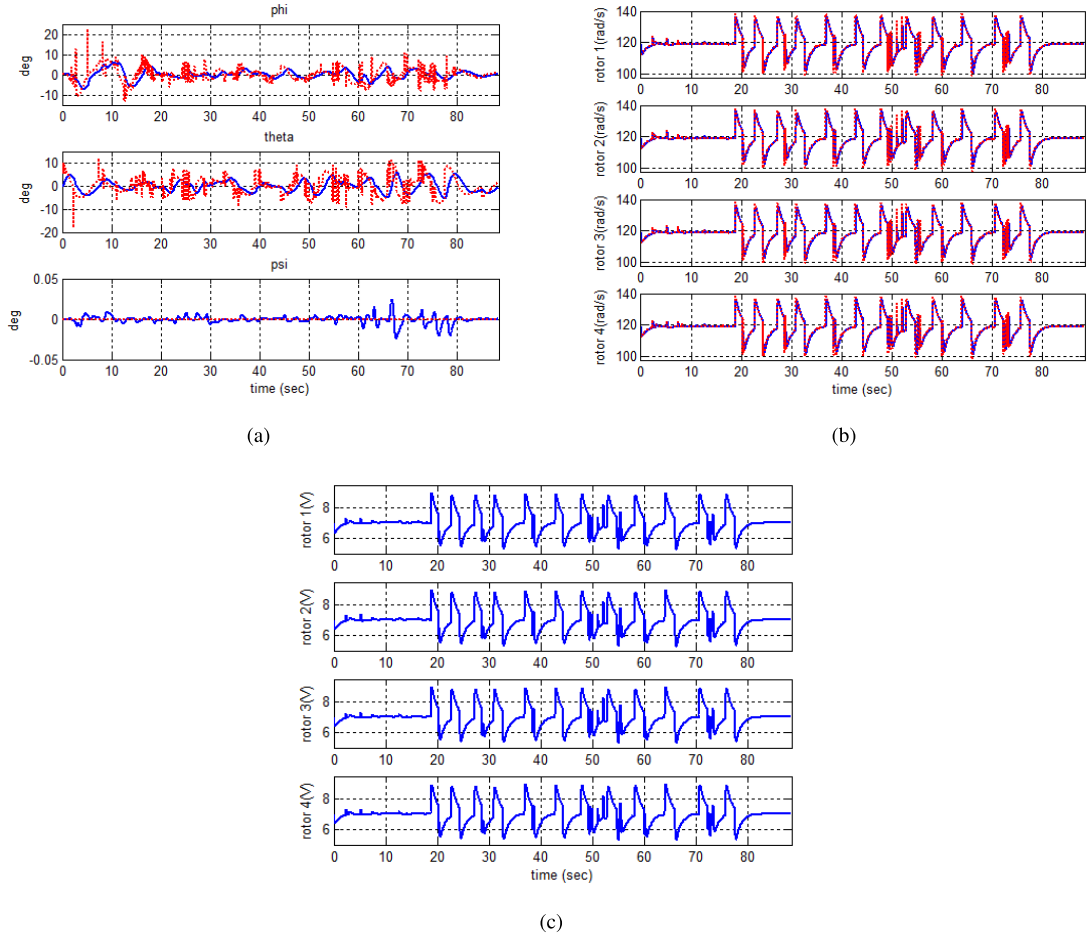


Fig. 15. Time histories (Case 1). (a) Roll, pitch, and yaw angles. (b) Rotor angular velocity. (c) Control input.

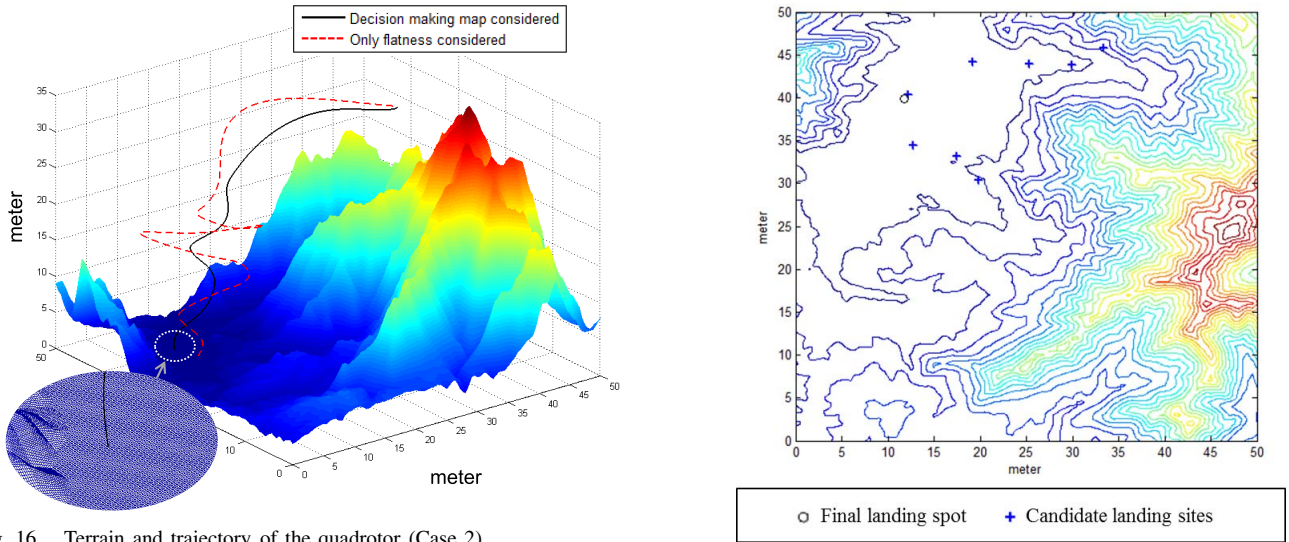


Fig. 16. Terrain and trajectory of the quadrotor (Case 2).

In this paper, upper left and lower right vertices' components of the rectangular image plane are chosen. If there exists intersection between the current image plane and any discarded region in the previous process, then the intersected area must be ruled out. The searching algorithm is summarized in Fig. 12.

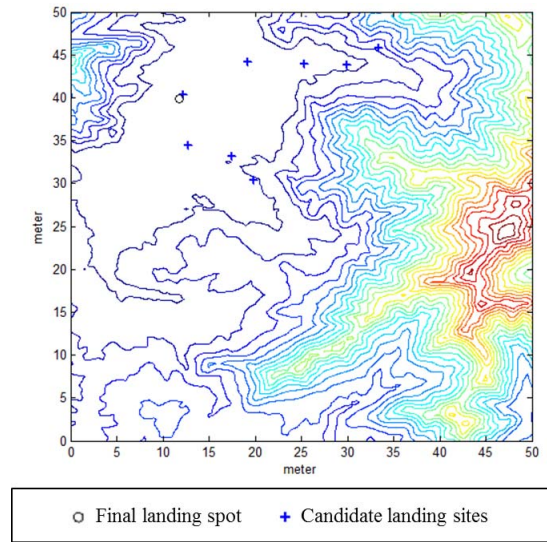


Fig. 17. Contour map (Case 2).

E. Final Landing Condition and Waypoint Guidance Law

If the primary candidate landing site is found, then the quadrotor stops searching and lands on the landing spot immediately. Altitude needs to be low enough for the disparity to be D_{n-1} . As mentioned in the previous section, D_n must be

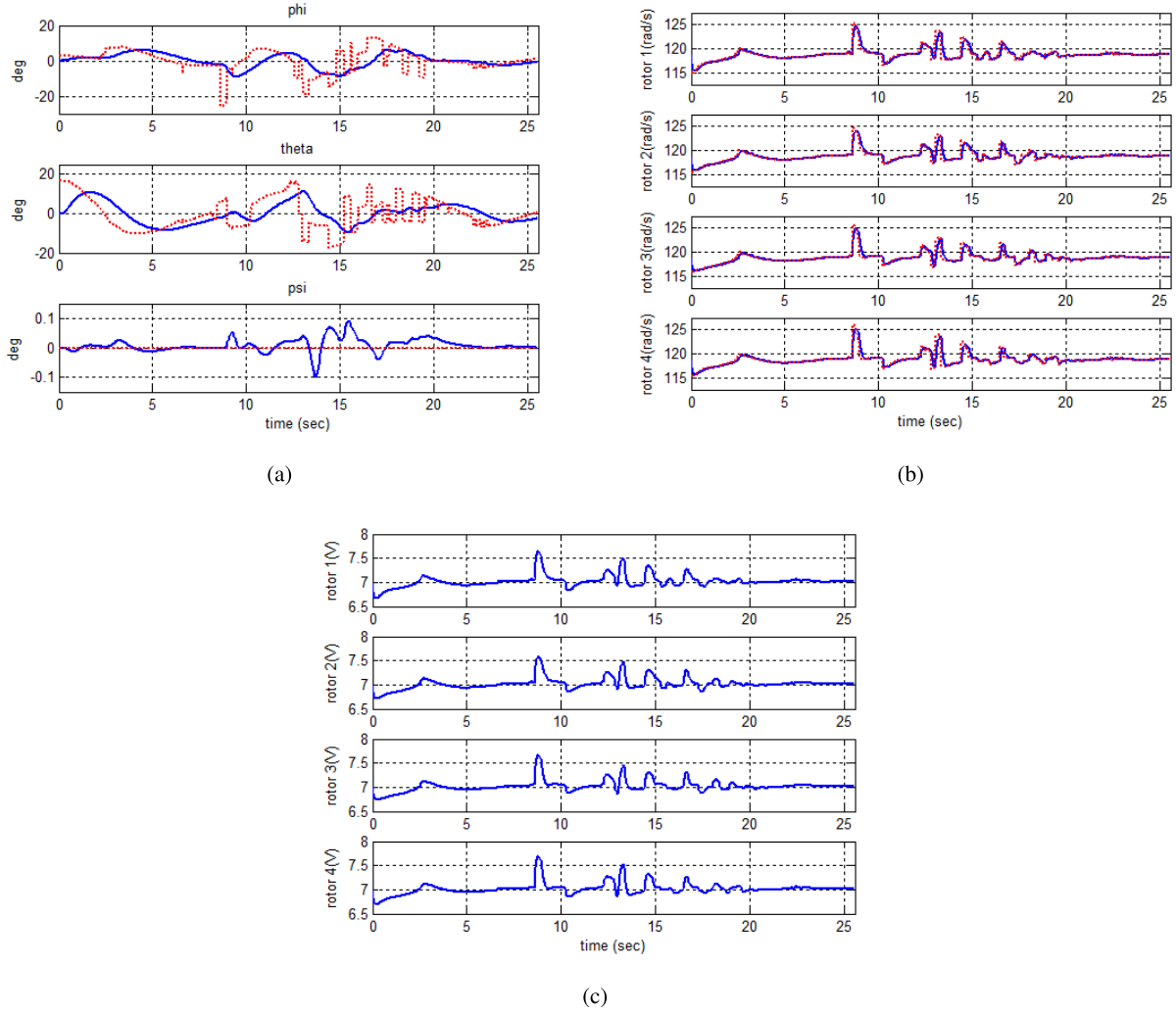


Fig. 18. Time histories (Case 2). (a) Roll, pitch, and yaw angles. (b) Rotor angular velocity. (c) Control input.

excluded. D_{n-1} guarantees that the slope of the landing area is not steep for the quadrotor to prevent slipping. In addition, the area of D_{n-1} must be wide enough to cover the entire quadrotor. If these two conditions are satisfied, then the position is chosen as desired landing site for the quadrotor to be guided.

In this paper, a conventional waypoint guidance algorithm [46], [47] is used to evaluate the proposed landing site search algorithm.

IV. NUMERICAL SIMULATION AND ANALYSIS

A. Simulation Environments

To verify the performance of the proposed algorithm, three topographies, rough sinusoid topography, mountain topography, and urban topography, are considered. In this paper, full dynamics summarized in Appendix A is considered to design a control system. Feedback linearization technique is adopted to deal with the nonlinearity of the quadrotor dynamics [44]. The method transforms original nonlinear eqnarrays into equivalent linear equations. This can be done by changing the state variables and the control inputs

to appropriate ones. In this paper, the gyroscopic torque term is ignored due to its little effect on the whole dynamic system. By a numerical simulation, it is confirmed that the magnitude of the gyroscopic torque is 10^{-8} to 10^{-15} order while the magnitude of the other two torques is 10^{-3} to 10^{-7} order, and the gyroscopic torque is always about 10^4 times less than the other two torques. To control the transformed linear system, two linear quadratic trackers are designed [45]. The purpose of the linear quadratic tracker is to make the output follow the desired output. In the attitude control subsystem, the desired outputs are three attitude angles of the quadrotor where two of them are provided by the position control subsystem. In addition, in the position control subsystem, the desired output is the position vector of the waypoint. In linear quadratic tracker, the weighting matrices of state error vector and control input error vector of the attitude control subsystem are taken as $Q_a = \text{diag}[10, 10, 10, 10, 10, 10]$ and $R_a = \text{diag}[1, 1, 1]$, respectively. In addition, those of the position control subsystem are taken as $Q_p = \text{diag}[1, 1, 1, 1, 1, 1]$ and $R_p = \text{diag}[10, 10, 10]$, respectively. The weighting parameters of the decision making map, i.e., c_1 , c_2 , and c_3 , are set to 0.2, 0.6, and 0.2, respectively. The parameters

TABLE V
PARAMETERS OF THE QUADROTOR AND THE STEREO VISION

Quadrotor				Stereo vision	
m	$0.65kg$	k_{tx}	$2kg/s$	J_x	$7.5e^{-3}kgm^2$
ρ	$1.293kg/m^3$	k_{ty}	$2kg/s$	J_y	$7.5e^{-3}kgm^2$
C_T	0.055	k_{tz}	$4kg/s$	J_z	$1.3e^{-2}kgm^2$
C_Q	0.024	k_{rx}	$1.5e^{-1}kgm^2/s$	d	$0.25m$
R	$0.15m$	k_{ry}	$1.5e^{-1}kgm^2/s$	g	$9.81m/s^2$
A	$0.0707m^2$	k_{rz}	$1.5e^{-1}kgm^2/s$	V_g	14V
k_m	$1.433e^{-2}kgm^2/s^2A$	J_m	$4e^{-4}kgm^2$	R_m	0.036Ω
k_d	$1.5e^{-4}kgm^2$	J_r	$6e^{-4}kgm^2$	k_e	$1.433e^{-2}Vs$

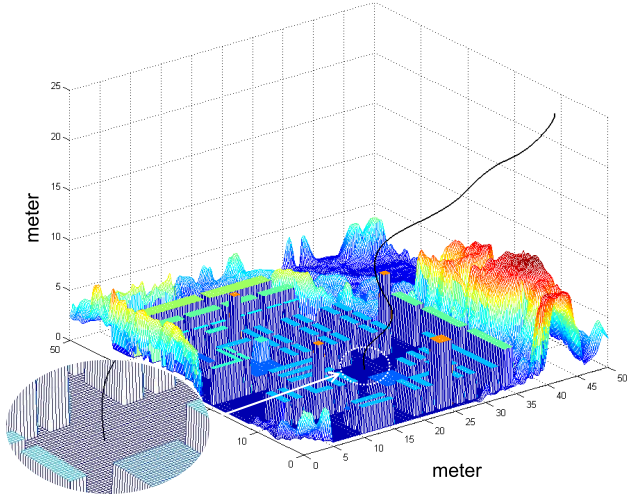


Fig. 19. Terrain and trajectory of the quadrotor (Case 3).

of the quadrotor and the stereo vision used in the simulation are summarized in Table V, and ψ_d is set to 0° . For practical implementation, experimental systems are constructed and introduced in Appendix B. The hardware system includes vision system, flight control system, and quadrotor system.

B. Case 1: Rough Sinusoid Topography

For the first case, the considered terrain is analogous to a sine curve, which is a synthetic image for the verification of the proposed algorithm. Fig. 13 shows the topography with the trajectory of the quadrotor, and Fig. 14 shows the corresponding contour map, which is a top view of Fig. 13. The terrain has four large candidate landing holes, as shown in Fig. 13. Two of them (candidates 2 and 4) are designed as a flat area, whereas the others (candidates 1 and 3) are too rough for a quadrotor to be landed, as shown in Figs. 13 and 14.

Initial position of the quadrotor is set to $[15 \ 25 \ 25]^T$ from which the stereo vision can detect only a rough hole. Therefore, the quadrotor falls into the rough hole at first and finds out that it is one of ruled-out regions, as shown

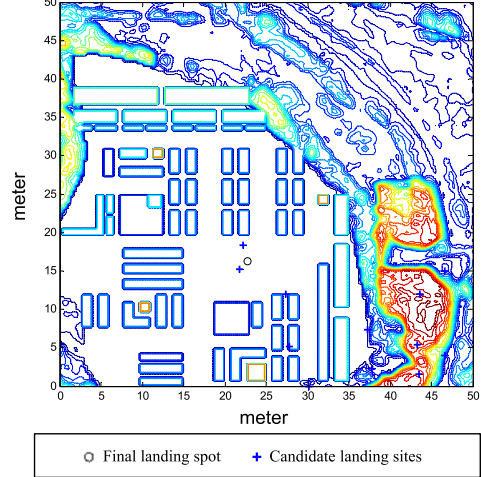


Fig. 20. Contour map (Case 3).

in Fig. 14, which means it is not an appropriate area for landing. Then, the quadrotor increases its altitude to move to the location stored in candidate landing sites. As soon as the quadrotor detects the area right next to ruled-out regions, the quadrotor tries to land on the area. However, after decreasing its altitude, the quadrotor recognizes that the area is also impossible to land due to the coarseness of the entire hole. After the whole rough region is marked as ruled-out regions, the quadrotor tries to find another hole, which is flat and lands safely.

Fig. 15(a)–(c) shows the attitude angles of the quadrotor, rotor angular velocity, and control input [pulsewidth modulation (PWM) voltage], respectively. Dotted lines in Fig. 15(a) and (b) are commands from the control input, and solid lines are the actual responses. The difference between these two responses results from the actuator dynamics that makes the actual responses physically realizable. Note from Fig. 15(a) that ϕ and θ are nearly zero degree at the final stage, which means that the quadrotor is stable enough to land safely. This simulation result verifies that the quadrotor is capable of detecting a rough area, recognizing it as ruled-out regions, and performing safe landing eventually.

TABLE VI
RESULT OF SIMULATION TIME AND ENERGY CONSUMPTION (CASE 2)

	Total simulation time	Total energy consumption ($kg \cdot m^2/s^2$)
Only flatness considered [53]	37.25s	242.5632
Decision making map considered	25.55s	163.0695

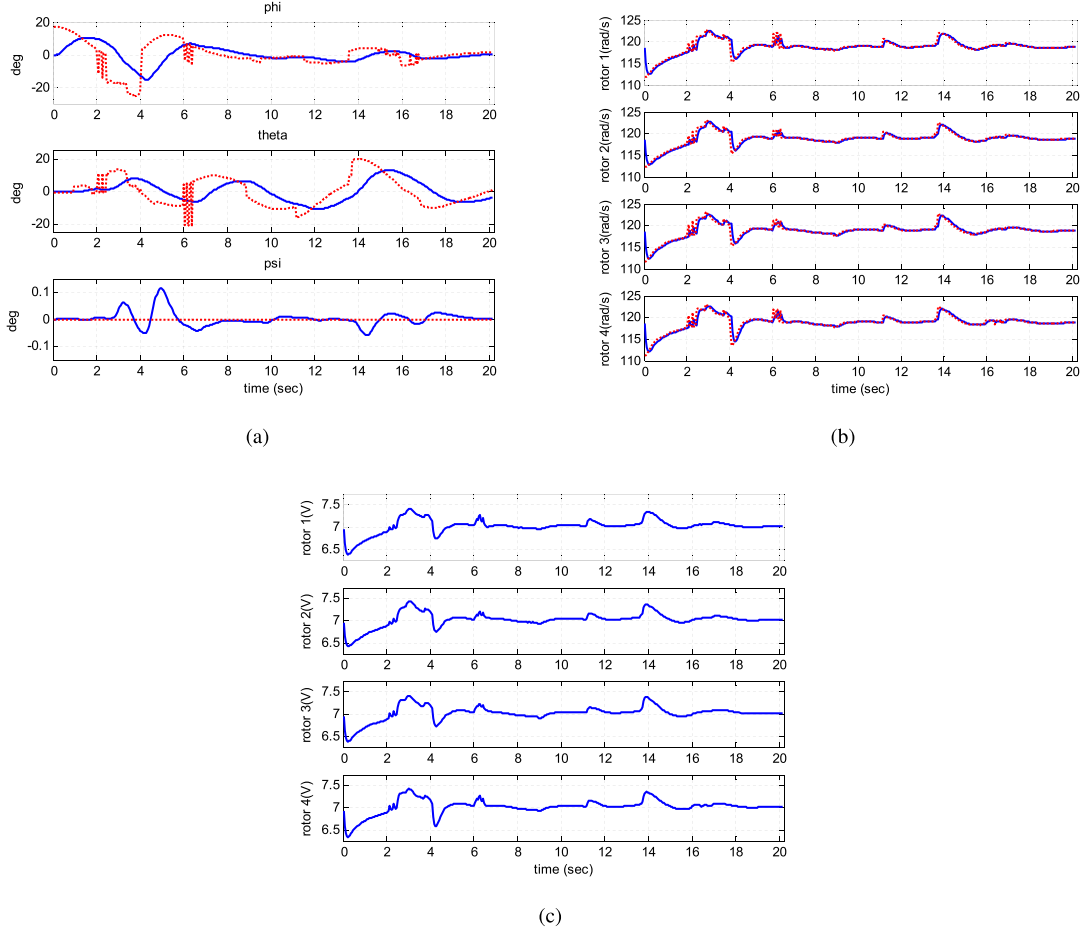


Fig. 21. Time histories (Case 3). (a) Roll, pitch, and yaw angles. (b) Rotor angular velocity. (c) Control input.

C. Case 2: Mountain Topography

For the second case, a mountain area is considered where a small portion of the area is flat. Initial position of the quadrotor is set to $[30 \ 40 \ 30]^T$. In the beginning, the quadrotor is in the status where the cameras cannot find a flat area. Fig. 16 shows the terrain and the trajectory of the quadrotor. In Fig. 16, solid line shows the trajectory produced using the decision making map and dashed line [53] shows the trajectory considering only the flatness information. Fig. 17 shows the corresponding contour map with a final spot and several candidate landing sites. In this case, ruled-out regions do not occur.

As shown in Table VI, the performance of the proposed algorithm is significantly improved both in the simulation time and the energy consumption by considering the combined decision making map in deciding the landing spot. Unnecessary movements of the quadrotor is reduced during the

search period, as shown in Fig. 16. When only the flatness information is considered, the quadrotor tries to move to the spot no matter how far it is located from the current position. This results in a lot of movements of the quadrotor, and consequently the quadrotor consumes more time and energy to find the final landing spot. However, by considering the combined decision making map proposed in this research, the importance of the distance between the landing spot and the position of the quadrotor is emphasized. Therefore, the movement of the quadrotor is reduced that leads to consuming less time and energy. Fig. 18(a)–(c) shows the time responses of the attitude of the quadrotor, rotor angular velocity, and control input, respectively.

D. Case 3: Urban Topography

For the third case, an urban topography is considered where a lot of quadrotor missions may be performed. As shown

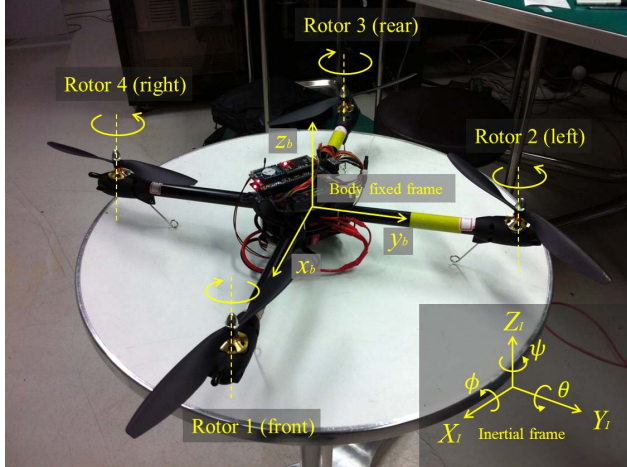


Fig. A.1. Quadrotor and coordinate system.

in Fig. 19, the terrain is surrounded by a mountain that is not appropriate for landing. The other part is a flat area where various buildings exist. Initial position of the quadrotor is set to $[5 \ 45 \ 25]^T$. Fig. 19 shows the terrain and the trajectory of the quadrotor and the corresponding contour with a final spot and several candidate landing sites is shown in Fig. 20. Even though the candidate landing sites are found on the mountain topography, as shown in Fig. 20, the candidate landing sites on the urban area have higher scores. Therefore, the quadrotor moves to the urban area and lands safely on the flat area. Fig. 21 shows the time responses of the attitude of the quadrotor, rotor angular velocity, and control input, respectively.

V. CONCLUSION

In this paper, stereo vision-based landing site searching algorithm was proposed. Quadrotor dynamic modeling was developed especially considering the nonlinear effect. Feedback linearization technique was adopted, and linear quadratic trackers were used to design controllers. A camera-based stereo vision sensor was considered to obtain the depth information. Canny edge detector and Euclidean distance transform were also adopted to acquire flatness information from the depth map. Depth map, flatness map, and energy consumption map were finally combined to select the most appropriate spot for landing. The performance of the proposed algorithm was verified through the numerical simulation and it demonstrated a significant improvement both in computation time and energy consumption. Hardware system constructed for practical implementation was also introduced, which includes vision system, flight control system, and quadrotor system. Future work includes obstacle detection for the safety of the quadrotor during the search of a landing site. In addition, an embedded system mounted on the real quadrotor will be implemented to validate the proposed algorithm via flight test.

APPENDIX A QUADROTOR SYSTEM MODELING

Quadrotor is configured in a way that two pairs of rotors, i.e., front and rear rotors, and the left and right rotors, rotate in

TABLE B.I
DETAILS OF VISION SYSTEM SPECIFICATIONS

Vision system	
Hardware	Bumblebee2
Software	FlyCapture SDK & Triclops SDK
Port	IEEE 1394
Focal length	3.8mm
Baseline	12cm
Horizontal field of view	65°
Computational rate	15Hz

an opposite direction, as shown in Fig. A.1. By controlling the speed of the rotors, the desired motion of the quadrotor can be achieved. Based on the earlier works [38], [41], [42], [46], the following translational and rotational dynamics of the quadrotor is developed in this research:

$$\ddot{\mathbf{p}} = -\frac{1}{m} R_{I/B}^t K_t (R_{I/B}^t)^{-1} \dot{\mathbf{p}} - G + \frac{1}{m} R_{I/B}^t F_t \quad (\text{A.1})$$

$$\begin{aligned} \ddot{\Phi} = & -(R_{B/I}^r)^{-1} J^{-1} K_r R_{B/I}^r \dot{\Phi} - (R_{B/I}^r)^{-1} J^{-1} (R_{B/I}^r \dot{\Phi}) \\ & \times (J R_{B/I}^r \dot{\Phi}) - (R_{B/I}^r)^{-1} \left(\frac{\partial R_{B/I}^r}{\partial \theta} \dot{\theta} + \frac{\partial R_{B/I}^r}{\partial \psi} \dot{\psi} \right) \dot{\Phi} \\ & - (R_{B/I}^r)^{-1} J^{-1} \sum_{i=1}^4 J_r ((R_{B/I}^r \dot{\Phi}) \times \hat{e}_3) (-1)^{i+1} w_i \\ & + (R_{B/I}^r)^{-1} J^{-1} T_t \end{aligned} \quad (\text{A.2})$$

where $\mathbf{p} \equiv [x \ y \ z]^T$ and $\Phi \equiv [\phi \ \theta \ \psi]^T$ are position vector and attitude angle vector of the quadrotor expressed in the inertial frame, respectively, m and J are mass and inertial matrix of the quadrotor, respectively, K_t and K_r are aerodynamic friction matrix of the force and the torque, respectively, F_t and T_t are force and torque produced by the rotor system of the quadrotor, respectively, G is a gravity acceleration vector, J_r is a rotor inertia, \hat{e}_3 is $[0 \ 0 \ 1]^T$, \times is a cross product of two vectors, and w is an angular velocity of the rotor. $R_{I/B}^t$ and $R_{B/I}^r$ are transformation matrix from the body fixed frame to the inertial frame and rotation velocity matrix from the inertial frame to the body fixed frame, respectively. In coordinate transformation, Euler angles of (1–2–3) rotation are used because of the convenience of controlling position dynamics.

External forces considered in modeling are thrust force, aerodynamic force, and gravitational force. In addition, external torques are torque produced by thrust, torque produced by aerodynamics, and gyroscopic torque. In (A.2), the gyroscopic torque term is especially considered that is caused by the rotation of the quadrotor with the rotating rotors [41], [42].

In this paper, brushless direct current [43] is adopted to model the nonlinear actuator dynamics as follows:

$$\dot{w}_i = -\frac{k_m k_e}{J_m R_m} w_i - \frac{k_d}{J_m} w_i^2 + \frac{k_m}{J_m R_m} V_g \text{sat}_{\delta_2}(d z_{\delta_1}(\delta_i)) \quad i \in \{1, 2, 3, 4\} \quad (\text{A.3})$$

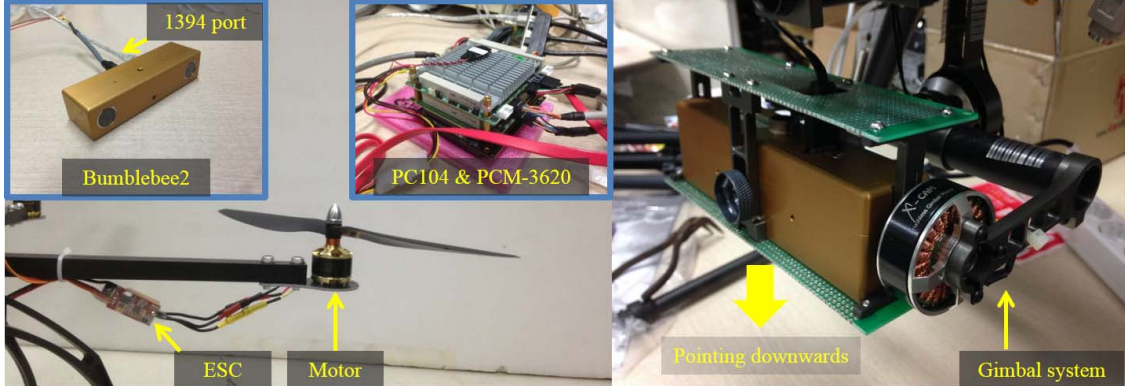


Fig. B.1. Experimental setup.

TABLE B.II

DETAILS OF FLIGHT CONTROL SYSTEM SPECIFICATIONS

Flight control system	
Embedded board	PCM-3362 PC104 & PCM-3620
CPU	1.62GHz
RAM	2GB
Data storage device	128GB solid state drive
Operating system	Windows 7
Computational rate	50Hz

TABLE B.III
DETAILS OF QUADROTOR SPECIFICATIONS

Quadrotor system	
Motor	GAUI 1050KV GUEC GM-410
Propeller	10 × 4.5 inch
Electronic speed controller (ESC)	GAUI GUEC GE-183 500X-18A
Battery	4400mAh 3S Lithium Polymer
Attitude and heading reference system	XSENS MTi
Maximum flight time	7min

where V_g is a terminal PWM voltage, $\delta \in [0, 1]$ is an input signal, R_m is a resistance, k_m , k_d , k_e are a motor torque constant, a load torque constant, and a back electromotive force constant, respectively, J_m is an inertia of the motor, $\text{sat}(\cdot)$ and $dz(\cdot)$ are saturation and deadzone function, respectively, and δ_1 and δ_2 are deadzone and saturation limits, respectively. In this research, both saturation and deadzone associated with nonlinearity are considered in depth. See [43] for an explanation of (A.3).

APPENDIX B HARDWARE SYSTEM

Experimental system is shown in Fig. B.1, which is currently being developed for practical implementation, i.e., flight test. The specifications for vision system, flight control system, and quadrotor system are summarized in Tables B.I–III.

REFERENCES

- [1] U.S. Military Unmanned Aerial Vehicles (UAV) Market Forecast 2013–2018, Market Research Media, San Francisco, CA, USA, 2012.
- [2] M. DeGarmo and G. M. Nelson, “Prospective unmanned aerial vehicle operations in the future national airspace system,” in *Proc. AIAA Aviation Technol., Integr. Oper. (ATIO) Forum*, Chicago, IL, USA, Sep. 2004.
- [3] C. S. Sharp, O. Shakernia, and S. S. Sastry, “A vision system for landing an unmanned aerial vehicle,” in *Proc. IEEE Int. Conf. Robot. Autom.*, Seoul, Korea, May 2001, pp. 1720–1727.
- [4] G. L. Carman, D. G. Ives, and D. K. Geller, “Apollo-derived Mars precision lander guidance,” in *Proc. AIAA Atmos. Flight Mech. Conf.*, Boston, MA, USA, Aug. 1998.
- [5] G. Welberg and B. K. Birge, “Terminal guidance techniques for a Mars precision lander,” in *Proc. AIAA Space Conf. Expo.*, Long Beach, CA, USA, Sep. 2000.
- [6] J. Gil-Fernandez, S. Melloni, P. Colmenarejo-Matellano, and M. Graziano, “Optimal precise landing for lunar missions,” in *Proc. AIAA/AAS Astrodyn. Specialist Conf.*, Honolulu, HI, USA, Aug. 2008.
- [7] B. E. Cohen and B. K. Collins, “Landing point designation algorithm for lunar landing,” *J. Spacecraft Rockets*, vol. 46, no. 4, pp. 858–864, 2009.
- [8] J. Delaune, D. D. Rosa, and S. Hobbs, “Guidance and control system design for lunar descent and landing,” in *Proc. AIAA Guid., Navigat., Control Conf.*, Toronto, ON, Canada, Aug. 2010.
- [9] S. E. Strandmoe, T. Jean-Marius, and S. Trinh, “Toward a vision based autonomous planetary lander,” in *Proc. AIAA Guid., Navigat., Control Conf.*, Portland, OR, USA, Aug. 1999.
- [10] L. Matthies, A. Huertas, Y. Cheng, and A. Johnson, “Landing hazard detection with stereo vision and shadow analysis,” in *Proc. AIAA Infotech Aerosp. Conf.*, Rohnert Park, CA, USA, May 2007.
- [11] B. Parreira *et al.*, “Consolidated performance assessment of hazard avoidance techniques for vision based landing,” in *Proc. AIAA Guid., Navigat., Control Conf.*, Hilton Head, SC, USA, Aug. 2007.
- [12] A. J. Sinclair and N. G. Fitz-Coy, “Comparison of obstacle avoidance strategies for Mars landers,” *J. Spacecraft Rockets*, vol. 40, no. 3, pp. 388–395, 2003.
- [13] S. P. Chakraborty, O. Aboutalib, and C. J. Meade, “Autonomous lunar lander hazard detection and avoidance system,” in *Proc. AIAA Space Conf. Expo.*, Pasadena, CA, USA, Sep. 2009.
- [14] E. P. Bonfiglio, D. Adams, L. Craig, D. A. Spencer, R. Arvidson, and T. Heet, “Landing-site dispersion analysis and statistical assessment for the Mars Phoenix Lander,” *J. Spacecraft Rockets*, vol. 48, no. 5, pp. 784–797, 2011.
- [15] G. B. Chatterji, P. K. Menon, and B. Sridhar, “Vision-based position and attitude determination for aircraft night landing,” *J. Guid., Control, Dyn.*, vol. 21, no. 1, pp. 84–92, 1998.
- [16] P. Trisiripisal, M. R. Parks, A. L. Abbott, and T. Liu, and G. A. Fleming, “Stereo analysis for vision-based guidance and control of aircraft landing,” in *Proc. AIAA Aerosp. Sci. Meeting*, Reno, NV, USA, Jan. 2006.
- [17] H. W. Schulz, M. Buschmann, L. Kruger, S. Winkler, and P. Vorsmann, “Towards vision-based autonomous landing for small UAVs—First experimental results of the vision system,” *J. Aerosp. Comput., Inf., Commun.*, vol. 4, no. 5, pp. 785–797, 2007.
- [18] B. Barber, T. McLain, and B. Edward, “Vision-based landing of fixed-wing miniature air vehicles,” *J. Aerosp. Comput., Inf., Commun.*, vol. 6, no. 3, pp. 207–226, 2009.

- [19] P. J. Garcia-Padro, G. S. Sukhatme, and J. F. Montgomery, "Towards vision-based safe landing for an autonomous helicopter," *Robot. Auto. Syst.*, vol. 38, no. 1, pp. 19–29, 2001.
- [20] S. Saripalli, J. F. Montgomery, and G. S. Sukhatme, "Visually guided landing of an unmanned aerial vehicle," *IEEE Trans. Robot. Autom.*, vol. 19, no. 3, pp. 371–380, Jun. 2003.
- [21] S. Saripalli, "Vision-based autonomous landing of an helicopter on a moving target," in *Proc. AIAA Guid., Navigat., Control Conf.*, Chicago, IL, USA, Aug. 2009.
- [22] M. Majji *et al.*, "Terrain mapping and landing operations using vision based navigation systems," in *Proc. AIAA Guid., Navigat., Control Conf.*, Portland, OR, USA, Aug. 2011.
- [23] P. T. Millet, B. B. Ready, and T. W. McLain, "Vision-based precision landings of a tailsitter UAV," in *Proc. AIAA Guid., Navigat., Control Conf.*, Chicago, IL, USA, Aug. 2009.
- [24] D. Fitzgerald and R. Walker, "Classification of candidate landing sites for UAV forced landings," in *Proc. AIAA Guid., Navigat., Control Conf.*, San Francisco, CA, USA, Aug. 2005.
- [25] S. Bayraktar and E. Feron, "Aggressive landing maneuvers for 3DOF helicopter UAV," in *Proc. AIAA Guid., Navigat., Control Conf.*, Keystone, CO, USA, Aug. 2006.
- [26] A. Johnson and M. SanMartin, "Motion estimation from laser ranging for autonomous comet landing," in *Proc. IEEE Int. Conf. Robot. Autom.*, San Francisco, CA, USA, Apr. 2000, pp. 132–138.
- [27] A. Johnson and T. Ivanov, "Analysis and testing of a LIDAR-based approach to terrain relative navigation for precise lunar landing," in *Proc. AIAA Guid., Navigat., Control Conf.*, Portland, OR, USA, Aug. 2011.
- [28] A. Mujumdar and R. Padhi, "Evolving philosophies on autonomous obstacle/collision avoidance of unmanned aerial vehicles," *J. Aerosp. Comput., Inf., Commun.*, vol. 8, no. 2, pp. 17–41, 2011.
- [29] R. J. Prazenica, A. Watkins, and A. J. Kurdila, "Vision-based Kalman filtering for aircraft state estimation and structure from motion," in *Proc. AIAA Guid., Navigat., Control Conf.*, San Francisco, CA, USA, Aug. 2005.
- [30] T. P. Webb, R. J. Prazenica, A. J. Kurdila, and R. Lind, "Vision-based state estimation for autonomous micro air vehicles," *J. Guid., Control, Dyn.*, vol. 30, no. 3, pp. 816–826, 2007.
- [31] M. Meingast, C. Geyer, and S. Sastry, "Vision based terrain recovery for landing unmanned aerial vehicles," in *Proc. 43rd IEEE Conf. Decision Control*, Atlantis, Bahamas, Dec. 2004, pp. 1670–1675.
- [32] A. D. Wu and E. N. Johnson, "Methods for localization and mapping using vision and inertial sensors," in *Proc. AIAA Guid., Navigat., Control Conf.*, Honolulu, HI, USA, Aug. 2008.
- [33] S. I. A. Shah, S. Kannan, and E. N. Johnson, "Motion estimation for obstacle detection and avoidance using a single camera for UAVs/robots," in *Proc. AIAA Guid., Navigat., Control Conf.*, Toronto, ON, Canada, Aug. 2010.
- [34] L. Pollini, F. Greco, R. Mati, M. Innocenti, and A. Tortelli, "Stereo vision obstacle detection based on scale invariant feature transform algorithm," in *Proc. AIAA Guid., Navigat., Control Conf.*, Hilton Head, SC, USA, Aug. 2007.
- [35] S. Hrabar, "3D path planning and stereo-based obstacle avoidance for rotorcraft UAVs," in *Proc. IEEE/RSJ Int. Conf. Intell. Robots Syst.*, Nice, France, Sep. 2008, pp. 807–814.
- [36] A. Bernatz and F. Thielecke, "Navigation of a low flying VTOL aircraft with the help of a downwards pointing camera," in *Proc. AIAA Guid., Navigat., Control Conf.*, Providence, RI, USA, Aug. 2004.
- [37] R. Madison, G. Andrews, and P. DeBitetto, "Vision-aided navigation for small UAVs in GPS-challenged environments," in *Proc. AIAA Infotech Aerosp. Conf.*, Rohnert Park, CA, USA, May 2007.
- [38] T. Bresciani, "Modelling, identification and control of a quadrotor helicopter," M.S. thesis, Dept. Autom. Control, Lund University, Lund, Sweden, Oct. 2008.
- [39] T. Sudiyanto, Muljowidodo, and A. Budiyono, "First principle approach to modeling of primitive quad rotor," *Int. J. Aeronautical Space Sci.*, vol. 10, no. 2, pp. 148–160, 2009.
- [40] A. R. S. Bramwell, G. Done, and D. Balmford, *Bramwell's Helicopter Dynamics*. Oxford, U.K.: Butterworth, 2001, pp. 1–114.
- [41] H. Bouadi, M. Bouchouche, and M. Tadjine, "Sliding mode control based on backstepping approach for an UAV type-quadrotor," *World Acad. Sci., Eng. Technol.*, vol. 20, no. 2, pp. 22–27, 2007.
- [42] T. Madani and A. Benallegue, "Backstepping control for a quadrotor helicopter," in *Proc. IEEE/RSJ Int. Conf. Intell. Robots Syst.*, Beijing, China, Oct. 2006, pp. 3255–3260.
- [43] A. S. Sanca, P. J. Alsin, and J. F. Cerqueira, "Dynamic modelling of a quadrotor aerial vehicle with nonlinear inputs," in *Proc. IEEE Latin Amer. Robot. Symp.*, Bahia, Brazil, Oct. 2008, pp. 143–148.
- [44] H. K. Khalil, *Nonlinear Systems*. Upper Saddle River, NJ, USA: Prentice-Hall, 2002, pp. 505–544.
- [45] B. L. Stevens and F. L. Lewis, *Aircraft Control and Simulation*, 2nd ed. Hoboken, NJ, USA: Wiley, 2003, pp. 403–481.
- [46] S. H. Lee, S. H. Kang, and Y. Kim, "Trajectory tracking control of quadrotor UAV," in *Proc. Int. Conf. Control Autom. Syst., ICCAS*, Gyeonggi-do, Korea, Oct. 2011, pp. 281–285.
- [47] H. Voos, "Nonlinear control of a quadrotor micro-UAV using feedback-linearization," in *Proc. IEEE Int. Conf. Mechatron.*, Malaga, Spain, Apr. 2009, pp. 1–6.
- [48] D. A. Forsyth and J. Ponce, *Computer Vision A Modern Approach*. Upper Saddle River, NJ, USA: Prentice-Hall, 2003, pp. 169–250.
- [49] J. Canny, "A computational approach to edge detection," *IEEE Trans. Pattern Anal. Mach. Intell.*, vol. PAMI-8, no. 6, pp. 679–698, Nov. 1986.
- [50] R. Maini and H. Aggarwal, "Study and comparison of various image edge detection techniques," *Int. J. Image Process.*, vol. 3, no. 1, pp. 1–12, 2009.
- [51] H. Breu, J. Gil, D. Kirkpatrick, and M. Werman, "Linear time Euclidean distance transform algorithms," *IEEE Trans. Pattern Anal. Mach. Intell.*, vol. 17, no. 5, pp. 529–533, May 1995.
- [52] D. E. Kirk, *Optimal Control Theory An Introduction*. Englewood Cliffs, NJ, USA: Prentice-Hall, 1970, pp. 259–291.
- [53] J. Park and Y. Kim, "Landing site searching algorithm of a quadrotor using depth map of stereo vision on unknown terrain," in *Proc. AIAA Infotech Aerosp. Conf.*, Garden Grove, CA, USA, Jun. 2012.



Jongho Park received the B.S. and M.S. degrees from the Department of Mechanical and Aerospace Engineering, Seoul National University, Seoul, Korea, in 2010 and 2012, respectively, where he is currently pursuing the Ph.D. degree.

His current research interests include applications of vision sensors in unmanned aerial vehicles (UAVs), vision-based guidance and control of UAVs, and control and load relief of launch vehicles.



Youdan Kim (M'94) received the B.S. and M.S. degrees in aeronautical engineering from Seoul National University, Seoul, Korea, in 1983 and 1985, respectively, and the Ph.D. degree in aerospace engineering from Texas A&M University, College Station, TX, USA, in 1990.

He joined the faculty of the Seoul National University in 1992, where he is currently a Professor with the Department of Mechanical and Aerospace Engineering. His current research interests include control system design for aircraft and spacecraft, reconfigurable flight control system, and missile guidance and control.



Sungwan Kim (S'90–M'94–SM'00) received the B.S. degree in electronics engineering and the M.S. degree in control and instrumentation engineering from Seoul National University (SNU), Seoul, Korea, in 1985 and 1987, respectively, and the Ph.D. degree in electrical engineering from the University of California at Los Angeles, Los Angeles, CA, USA, in 1993.

He was with the Dynamic Systems and Control Branch, NASA Langley Research Center, Hampton, VA, USA, as a Senior Researcher, prior to joining SNU. He has led the research team as a Principal Engineer with Boeing Company, Huntington Beach, CA, USA, since 1997, and has been a Professor with the Department of Biomedical Engineering, College of Medicine, SNU, since 2010. His current research interests include early detection, medical robot, and biomedical control and modeling.

Dr. Kim is an Associate Fellow of the American Institute of Aeronautics and Astronautics. He has served as an Associate Editor of the IEEE TRANSACTIONS ON BIOMEDICAL ENGINEERING and the IEEE TRANSACTIONS ON CONTROL SYSTEMS TECHNOLOGY journals for over 10 years.